

## ARTICLE OPEN



## Size-dependent aerosol iron solubility in an urban atmosphere

Lei Liu<sup>1</sup>, Weijun Li<sup>1</sup>✉, Qiuhan Lin<sup>1,2</sup>, Yue Wang<sup>1</sup>, Jian Zhang<sup>1,3</sup>, Yanhong Zhu<sup>1</sup>, Qi Yuan<sup>1,4</sup>, Shengzhen Zhou<sup>5</sup>, Daizhou Zhang<sup>6</sup>, Clarissa Baldo<sup>7</sup> and Zongbo Shi<sup>7</sup>✉

Size distribution of aerosol iron (Fe) concentration and solubility determines their environmental and health impacts but they are rarely reported. In this study, size-resolved aerosol particles were collected in Hangzhou, a Chinese megacity upwind of the Asian outflow to the Pacific Ocean. Total and dissolved Fe collected under non-haze, haze, and dust conditions were determined. Results show that total Fe concentrations displayed a unimodal distribution peaking at 3.2–5.6  $\mu\text{m}$  under non-haze and dust conditions, but a bimodal distribution under the haze condition peaking at 3.2–5.6  $\mu\text{m}$  and 0.32–0.56  $\mu\text{m}$ . Dissolved Fe under the non-haze, haze, and dust conditions all displayed bimodal size distributions with one peak in the fine-mode (0.056–1.0  $\mu\text{m}$ ) fraction and one peak in the coarse-mode (>1.0  $\mu\text{m}$ ) fraction. Fe enrichment factor in fine-mode particles under the haze condition is up to 17.8, suggesting a potential contribution from anthropogenic Fe. Fe solubility in total suspended particles under the haze condition (3.8%) is significantly higher than those under non-haze (2.6%) and particularly dust (0.5%) conditions. Furthermore, Fe solubilities in fine-mode particles under non-haze (10.8%) and haze (10.9%) conditions were much higher than those (1.5% and 2.4%) in coarse-mode particles. We found that Fe solubility was correlated positively with aerosol acidity and negatively with particle size from 0.32 to 5.6  $\mu\text{m}$ . Individual particle analysis further reveals that nanosized iron oxides were internally mixed with acidic sulfates/nitrates under the haze condition. Our results indicate that the strong size dependence of aerosol Fe solubility is associated with the differences in sources of aerosol Fe and its acidic processing.

npj Climate and Atmospheric Science (2022)5:53; <https://doi.org/10.1038/s41612-022-00277-z>

## INTRODUCTION

Iron (Fe), an essential micronutrient for oceanic primary productivity, modulates marine ecosystems, atmospheric carbon dioxide ( $\text{CO}_2$ ) uptake, and the global climate<sup>1,2</sup>. The deposition of atmospheric aerosol Fe to the remote ocean surface is an important external source of bioavailable Fe for plankton growth<sup>3–6</sup>. Fe in atmospheric particles can also affect human health because Fe in the atmosphere is considered to be one of the most important prerequisites for reactive oxygen species upon inhalation<sup>7</sup>. Aerosol Fe comes from natural mineral dust (e.g., soils or deserts) and anthropogenic fuel combustion sources (e.g., coal and biomass) in continental areas<sup>2,8–10</sup>. Mineral dust is estimated to represent 95% of the global atmospheric total Fe ( $\text{Fe}_T$ ) budget, with the remaining fraction attributed to anthropogenic emissions<sup>11,12</sup>. However, the anthropogenic activities were estimated to supply about 50% of dissolved Fe ( $\text{Fe}_D$ , considered as potentially bioavailable Fe) in oceans in the Northern Hemisphere<sup>13</sup>.

The Fe solubility ( $\text{Fe}_s$ , i.e., ratio of  $\text{Fe}_D$  to  $\text{Fe}_T$ ) is the main factor affecting the biogeochemical cycle of Fe<sup>14</sup>. It is well known that source, particle size, pollution level, and aerosol acidity can affect  $\text{Fe}_s$ <sup>15–17</sup>. The  $\text{Fe}_s$  of fresh mineral dust is usually less than 0.5%, whereas the solubilities of pyrogenic Fe are 1–2 orders of magnitude higher than those of mineral dust Fe even though the low contribution of pyrogenic sources to atmospheric  $\text{Fe}_T$ <sup>12</sup>. The observed  $\text{Fe}_s$  ranges from 1 to 80% in atmospheric aerosols depending on their different sources and weather conditions<sup>15,18–20</sup>. Studies suggest that most  $\text{Fe}_D$  is linked to the chemical processing of Fe-containing particles during long-range

transports<sup>13</sup>. This “chemical process” is generally thought to involve heterogeneous reactions between acidic species and Fe-containing particles, sunlight, and cloud water condensation/evaporation<sup>3,19,21,22</sup>. For example, Shi et al.<sup>18</sup> reported that insoluble Fe in mineral dust readily dissolves under acidic conditions relevant to wet aerosols; whereas, the activation of wet aerosols into cloud droplets halts the Fe dissolution. Although a large number of studies (e.g., refs. 15,16,23–27) have gained a certain understanding of the source, solubility, and mixing state of Fe in the atmosphere over cities through individual particle and bulk sample analyses, size-resolved characteristics of aerosol Fe and its solubility still need further investigation. The knowledge of aerosol Fe contents and solubilities among different particle sizes is important to understand their sources, chemical processes, and long-range transport characteristics, and to evaluate their air-to-sea deposition flux and human health effects.

It is reported that Fe-containing aerosols had a single-mode size distribution, dominated by coarse-mode particles under the ultraclean atmosphere on the Arctic Ocean and West Antarctic Peninsula, suggesting important contributions of regional and local dust sources<sup>17,28</sup>. As one of the world's largest city clusters located east coast of China, the Yangtze River Delta (YRD) is the main source region of anthropogenic aerosols transported to the East China Sea and even the Northwest Pacific Ocean following the northwesterly winter monsoon<sup>29</sup>. However, the study of size-resolved aerosol Fe in this region is limited. Therefore, it is necessary to study the size-resolved characteristics of aerosol Fe and its solubility in this region to better evaluate its influence on

<sup>1</sup>Key Laboratory of Geoscience Big Data and Deep Resource of Zhejiang Province, Department of Atmospheric Sciences, School of Earth Sciences, Zhejiang University, Hangzhou 310027, China. <sup>2</sup>Putian Weather Bureau, Putian 351100, China. <sup>3</sup>School of Environmental and Material Engineering, Yantai University, Yantai 264005, China. <sup>4</sup>College of Environmental Science and Engineering, Ocean University of China, Qingdao 266100, China. <sup>5</sup>School of Atmospheric Sciences and Guangdong Province Key Laboratory for Climate Change and Natural Disaster Studies, Sun Yat-sen University, Guangzhou 510275, China. <sup>6</sup>Faculty of Environmental and Symbiotic Sciences, Prefectural University of Kumamoto, Kumamoto 862-8502, Japan. <sup>7</sup>School of Geography, Earth and Environmental Sciences, University of Birmingham, Birmingham B15 2TT, UK.

✉email: liweijun@zju.edu.cn; z.shi@bham.ac.uk

**Table 1.** Concentrations of total Fe ( $Fe_T$ ), dissolved Fe ( $Fe_D$ ), and Fe solubility ( $Fe_S$ ) in total suspended, coarse-, and fine-mode particles, as well as the enrichment factor of Fe ( $EF_{Fe}$ ) in coarse- and fine-mode particles under non-haze, haze, and dust conditions.

Condition	Total suspended particles			Coarse-mode particles (>1.0 $\mu\text{m}$ )				Fine-mode particles (<1.0 $\mu\text{m}$ )			
	$Fe_T$ $\text{ng m}^{-3}$	$Fe_D$ $\text{ng m}^{-3}$	$Fe_S$ %	$Fe_T$ $\text{ng m}^{-3}$	$Fe_D$ $\text{ng m}^{-3}$	$Fe_S$ %	$EF_{Fe}$	$Fe_T$ $\text{ng m}^{-3}$	$Fe_D$ $\text{ng m}^{-3}$	$Fe_S$ %	$EF_{Fe}$
Non-haze	1140	29.7	2.6	1003	14.8	1.5	4.1	137	14.9	10.8	6.0
Haze	2035	78.3	3.8	1692	41.1	2.4	4.9	342	37.3	10.9	17.8
Dust	4883	24.6	0.5	4551	18.0	0.3	4.0	332	6.6	2.0	4.2

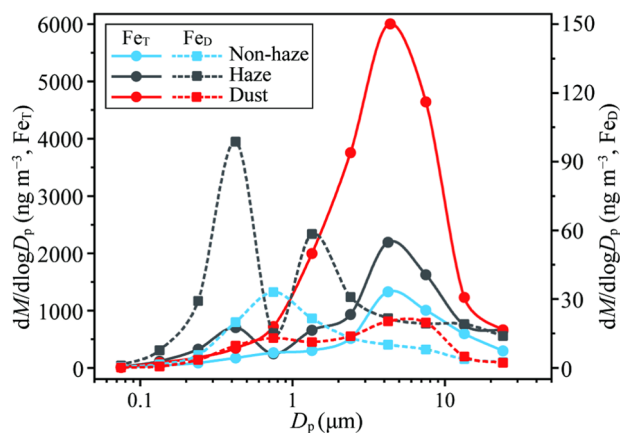


**Fig. 1** Mass-size distributions of aerosol total Fe ( $Fe_T$ , solid lines) and dissolved Fe ( $Fe_D$ , dashed lines). The particle size refers to the aerodynamic diameter ( $D_p$ ). The distributions under non-haze, haze, and dust conditions are indicated by blue, black, and red lines, respectively.

marine ecosystems. In this study, a 10-stage tandem impactor was used for sampling size-resolved aerosol particles under different weather conditions (i.e., non-haze, haze, and dust conditions) in Hangzhou, a megacity located in YRD. A variety of analytical methods were used to measure mass concentrations of aerosol  $Fe_T$ ,  $Fe_D$ , and acidic inorganic ions in different particle sizes and to characterize individual particles of aerosol Fe. We examined their relationships with acidic inorganic ions and further explored the solubilizing mechanisms of aerosol Fe.

## RESULTS AND DISCUSSION

### Aerosol Fe concentration and solubility in total suspended particulates

The concentrations and solubilities of aerosol Fe in total suspended particulate (TSP) under different conditions were obtained by summing the concentrations of  $Fe_T$  and  $Fe_D$  at each stage. The  $Fe_T$  and  $Fe_D$  concentrations in TSP under non-haze, haze, and dust conditions were 1140 and 29.7  $\text{ng m}^{-3}$ , 2035 and 78.3  $\text{ng m}^{-3}$ , and 4883 and 24.6  $\text{ng m}^{-3}$ , respectively (Table 1). The  $Fe_T$  in TSP had the highest concentration (4883  $\text{ng m}^{-3}$ ) under the dust condition, followed by haze (2035  $\text{ng m}^{-3}$ ) and non-haze (1140  $\text{ng m}^{-3}$ ) conditions (Table 1). However, the highest  $Fe_D$  concentration (78.3  $\text{ng m}^{-3}$ ) in TSP occurred under the haze condition, about 2.6 and 3.2 times those under non-haze (29.7  $\text{ng m}^{-3}$ ) and dust (24.6  $\text{ng m}^{-3}$ ) conditions, respectively (Table 1). Consequently, the calculated  $Fe_S$  in TSP under different conditions are in the following order: haze (3.8%) > non-haze (2.6%) > dust (0.5%) (Table 1).

### Mass-size distributions of aerosol Fe

Figure 1 shows the mass-size distributions of aerosol  $Fe_T$  and  $Fe_D$ .  $Fe_T$  showed unimodal size distributions with the peak at

3.2–5.6  $\mu\text{m}$  under non-haze and dust conditions.  $Fe_T$  concentrations in each size bin under the dust condition were 4–6 times higher than those under the non-haze condition. However,  $Fe_T$  under the haze condition showed a bimodal size distribution with a major peak at 3.2–5.6  $\mu\text{m}$  and a minor peak at 0.32–0.56  $\mu\text{m}$ , and its peak height at 3.2–5.6  $\mu\text{m}$  was 3.2 times that at 0.32–0.56  $\mu\text{m}$ .  $Fe_D$  under the non-haze, haze, and dust conditions all displayed bimodal size distributions with one peak in the fine-mode (0.056–1.0  $\mu\text{m}$ ) fraction and one peak in the coarse-mode (>1.0  $\mu\text{m}$ ) fraction. The size distribution of  $Fe_D$  showed a major peak at 0.56–1.0  $\mu\text{m}$  and a minor peak at 3.2–5.6  $\mu\text{m}$  under the non-haze condition, but a major peak at 3.2–5.6  $\mu\text{m}$  and a minor peak at 0.56–1.0  $\mu\text{m}$  under the dust condition. The size distribution of  $Fe_D$  under the haze condition displayed two major peaks at 0.32–0.56  $\mu\text{m}$  and 1.0–1.8  $\mu\text{m}$ . We noticed that the particle sizes corresponding to the two peaks of  $Fe_D$  in fine- and coarse-mode fractions under the haze condition were both smaller than those under non-haze and dust conditions, respectively.

$Fe_T$  concentrations in the coarse- and fine-mode fractions are 1003 and 137  $\text{ng m}^{-3}$  under the non-haze condition, 1692 and 342  $\text{ng m}^{-3}$  under the haze condition, and 4551 and 332  $\text{ng m}^{-3}$  under the dust condition, respectively (Table 1). The coarse-mode particles dominate  $Fe_T$  concentrations in aerosol particles under all three conditions (75–83%). On the other hand, the coarse-mode particles contributed 73% of the  $Fe_D$  under the dust condition (fine-mode 6.6  $\text{ng m}^{-3}$  vs coarse-mode 18.0  $\text{ng m}^{-3}$ ), but the  $Fe_D$  concentrations in coarse-mode particles were comparable to those in fine-mode particles under the non-haze (fine-mode 14.9  $\text{ng m}^{-3}$  vs coarse-mode 14.8  $\text{ng m}^{-3}$ ) and haze (fine-mode 37.3  $\text{ng m}^{-3}$  vs coarse-mode 41.1  $\text{ng m}^{-3}$ ) conditions (Table 1). The contribution of fine-mode particles to the  $Fe_D$  was larger than their contribution to the  $Fe_T$  under the non-haze and haze conditions. Therefore, although coarse-mode particles contributed the most to  $Fe_T$ , fine-mode particles contributed more to  $Fe_D$  in the aerosol particles.

We found that  $Fe_S$  in fine-mode particles reached relatively high values under the non-haze (10.8%) and haze (10.9%) conditions, which are 7.2 and 4.5 times those (non-haze 1.5% and haze 2.4%) in coarse-mode particles, respectively. In the contrary,  $Fe_S$  of fine-mode particles under the dust condition remained relatively low (2.0%) compared with that (0.3%) in coarse-mode particles (Table 1).

### Sources of aerosol Fe

In this study, the enrichment factor of element Fe ( $EF_{Fe}$ ) is used to evaluate the relative contribution of natural and anthropogenic sources to aerosol  $Fe_T$ . Table 1 shows that the  $EF_{Fe}$  in coarse-mode particles was 4.1, 4.9, and 4.0 under the non-haze condition, haze, and dust conditions. This suggests that aerosol Fe in coarse-mode particles mainly originated from crustal sources in all three cases. Coarse-mode particles under the non-haze and haze conditions are likely to be mainly from local sources, such as road traffic, construction, and soil surfaces in urban air<sup>30,31</sup>. The  $EF_{Fe}$  in fine-mode particles was 6.0 under the non-haze condition and 4.2 under the dust condition (Table 1), which indicates the dominant contribution from crustal sources. The  $EF_{Fe}$  in fine-mode particles under the haze condition was 17.8, suggesting that anthropogenic

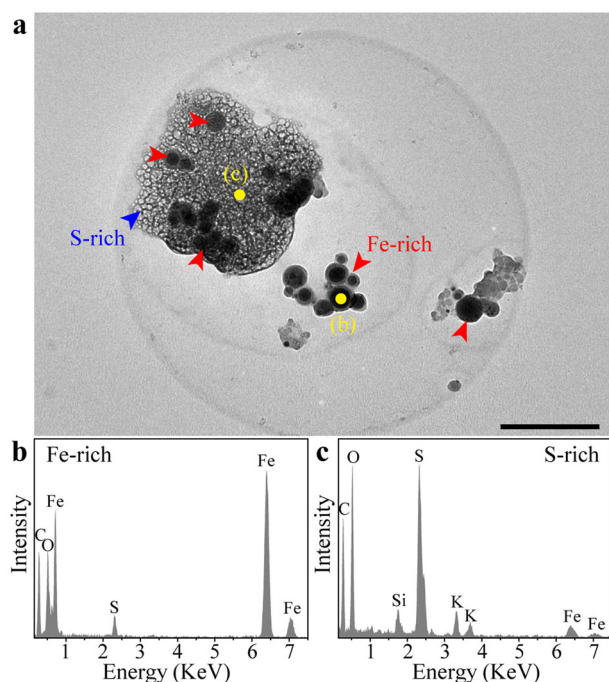


**Fig. 2** Typical TEM image and EDS spectra of anthropogenic Fe-containing particles. **a** typical TEM image showing the bare spherical Fe-rich particles or their aggregations and the internally mixed Fe-rich particles with secondary acidic aerosols (S-rich). **b** EDS spectrum of Fe-rich particle. **c** EDS spectrum of S-rich particle. The yellow dots (**b**) and (**c**) in panel **a** indicate the locations acquiring the EDS spectra in panels **b** and **c**, respectively. The scale bar in panel **a** is 500 nm.

sources contributed to  $Fe_T$  in fine-mode particles under the haze condition. This may explain the peak at 0.32–0.56  $\mu\text{m}$  in the mass-size distribution of  $Fe_T$  under the haze condition (Fig. 1).

It has been reported that the nanosized  $FeO_x$  particles are emitted from vehicles, industrial activities, and solid fuel burning in cities<sup>9,19,32</sup>. In this study, individual particle samples were analyzed using transmission electron microscopy (TEM) equipped with an energy-dispersive X-ray spectrometer (EDS). TEM-EDS showed aggregations of nanosized spherical Fe-rich particles (Fig. 2a). These particles mainly contain Fe and O (Fig. 2b), likely as  $FeO_x$  (e.g.,  $Fe_2O_3$  and  $Fe_3O_4$ ), which were identified to be from heavy industries with high-temperature combustion processes<sup>9,33</sup>. We observed a large number of spherical Fe-rich particles or their aggregates with diameters of 100–300 nm under the haze condition (Fig. 3a, b). Nanosized Fe-rich particles were also observed under the non-haze condition (Fig. 3c), which indicates the contribution of anthropogenic sources to aerosol Fe despite the dominance of crustal sources under the non-haze condition. As expected, a large number of coarse mineral particles containing Fe occurred under the dust condition (Fig. 3d). Individual particle analysis is in good agreement with the bulk analysis above with regards to the sources of aerosol Fe.

### Factors influencing aerosol Fe solubility

$Fe_5$  in fine-mode particles was much larger than that in coarse-mode particles (Table 1). This could be attributed to two possible reasons: (1) there are sources of aerosol Fe that have a much higher initial  $Fe_5$ , e.g., from combustion sources;<sup>12</sup> (2) heterogeneous reactions release more  $Fe_D$  in fine-mode particles, enhancing Fe solubility<sup>9</sup>. Recently, Zhu et al.<sup>15</sup> reported that the primary emissions of  $Fe_D$  in fine-mode particles could not explain  $Fe_5 > 3\%$  in Hangzhou. Here, the  $Fe_5$  in fine-mode particles was

much larger than 3% under non-haze (10.8%) and haze (10.9%) conditions (Table 1). Li et al.<sup>9</sup> provided indisputable evidence to demonstrate that anthropogenic  $FeO_x$  particles undergo heterogeneous reactions with acidic aerosols to produce  $Fe_D$  including iron sulfate or ferrous sulfate during atmospheric transport. Besides, Baldo et al.<sup>34</sup> reported that the anthropogenic pyrogenic Fe dissolves much faster than mineral dust under simulated atmospheric acid conditions. These results indicate that heterogeneous reactions likely contributed to the observed enhancement in  $Fe_5$  in fine-mode particles under the non-haze and haze conditions in Hangzhou.

To explore how acidification processes influence aerosol Fe solubility, we further explored the differences in  $Fe_5$  within the size range of 0.32–5.6  $\mu\text{m}$ . The degree of aerosol acidification is a key factor influencing the  $Fe_5$  in aerosol particles<sup>15</sup>. In this study, the molar ratio of  $(2SO_4^{2-} + NO_3^- - NH_4^+)/Fe_T$  was used to characterize the acidification degree of aerosols with respect to  $Fe_T$ <sup>16,35</sup>. Figure 4 shows the relationships between the  $Fe_5$  and degree of aerosol acidification as well as the particle size under the three cases. We found that  $Fe_5$  increased with the degree of aerosol acidification in the range of 0.32–5.6  $\mu\text{m}$  under all the conditions. However,  $Fe_5$  generally decreased with particle sizes in the range of 0.32–5.6  $\mu\text{m}$  except for the bins of 0.56–1.0  $\mu\text{m}$  under non-haze condition and 1.0–1.8  $\mu\text{m}$  under haze condition, which could be attributed to the higher degree of aerosol acidification in these two bins (Fig. 4 and Supplementary Fig. 1). The degree of aerosol acidification under the non-haze condition was larger than that under the haze condition, which may be ascribed to the increased gas-phase conversion efficiency of  $SO_2$  and  $NO_x$  to acid aerosol species due to the enhanced oxidizing capacity under the non-haze condition<sup>36,37</sup>. Therefore, the larger acidification degree caused a high Fe solubility comparable to that under the haze condition although crustal sources dominated under the non-haze condition. TEM observations further support the acidification effect. Some of the nanosized Fe-rich particles in the atmosphere were internally mixed with secondary acidic aerosols (e.g., S-rich particles in Figs. 2a and 3a–c) with diameters of 200–1000 nm under the haze and non-haze conditions, and the EDS spectrum displayed the presence of minor Fe in S-rich particles (Fig. 2c), which provides direct evidence for the possible heterogeneous reactions between  $FeO_x$  and acidic sulfates/nitrates. Such acidic species in the aerosol water can dissolve  $FeO_x$  particles into soluble iron sulfate and thereby promotes Fe dissolution<sup>9</sup>.

$Fe_5$  in the five size bins (i.e., 0.32–0.56  $\mu\text{m}$ , 0.56–1.0  $\mu\text{m}$ , 1.0–1.8  $\mu\text{m}$ , 1.8–3.2  $\mu\text{m}$ , and 3.2–5.6  $\mu\text{m}$ ) under the dust condition was significantly lower than those under the non-haze and haze conditions, respectively (Fig. 4 and Supplementary Fig. 1). Sun et al.<sup>38</sup> found that the mixed secondary aerosols (e.g., sulfate and nitrate) completely transform from a solid phase to a liquid phase when the relative humidity (RH) > 75% in the urban air. In this study, the average RH was 75% under the non-haze condition, 77% under the haze condition, and 54% under the dust condition (Supplementary Table 1). Thus, the surfaces of these secondary aerosols should be wet under the non-haze and haze conditions, which enhances the uptake of acidic gases (e.g.,  $SO_2$  and  $NO_2$ ) to produce acidic salts, e.g., sulfate and nitrate<sup>39,40</sup>. This enables the Fe transformation from insoluble Fe to soluble forms<sup>16,29,34,41,42</sup>.

### Atmospheric implications

Aerosol acidity is a key factor affecting aerosol Fe solubility<sup>43</sup>. However, aerosol acidity calculated from bulk  $PM_{2.5}$  composition can mask changes in the aerosol acidity with different particle sizes. Here, our size-resolved aerosol Fe solubility as shown in Fig. 4, together with TEM analyses as shown in Figs. 2 and 3 provided stronger support for the impact of aerosol acidity on Fe solubility.

We found that coarse-mode particles dominated the aerosol  $Fe_T$  but they had lower Fe solubility and fine-mode particles had

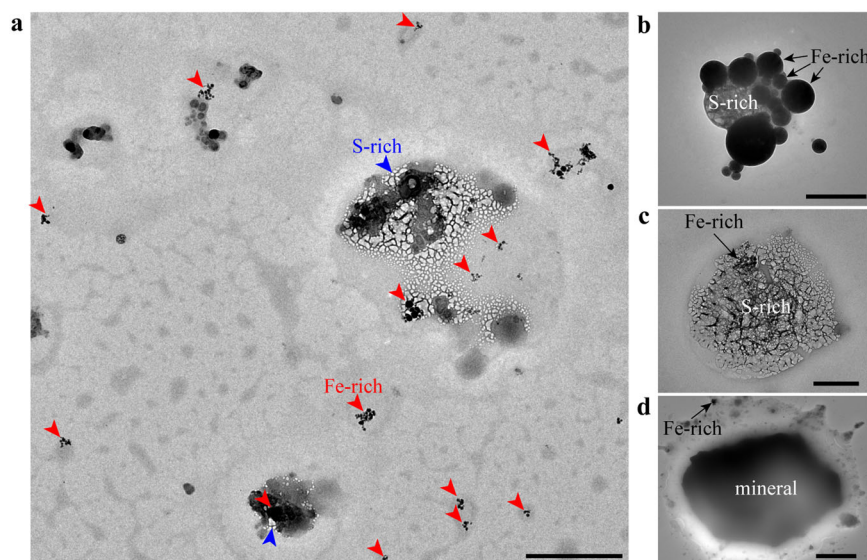


**Fig. 3 Morphology and mixing state of various Fe-containing particles collected under different conditions.** **a** Bare nanosized Fe-rich particles and internally mixed Fe-rich particles with secondary acidic aerosols (S-rich) collected under the haze condition. **b** Aggregation of nanosized Fe-rich particles associated with S-rich under the haze condition. **c** Nanosized Fe-rich particle internally mixed with S-rich collected under the non-haze condition. **d** Mineral dust particle-containing Fe collected under the dust condition. The scale bars are 500 nm in panels a–c and 2  $\mu\text{m}$  in panel d.

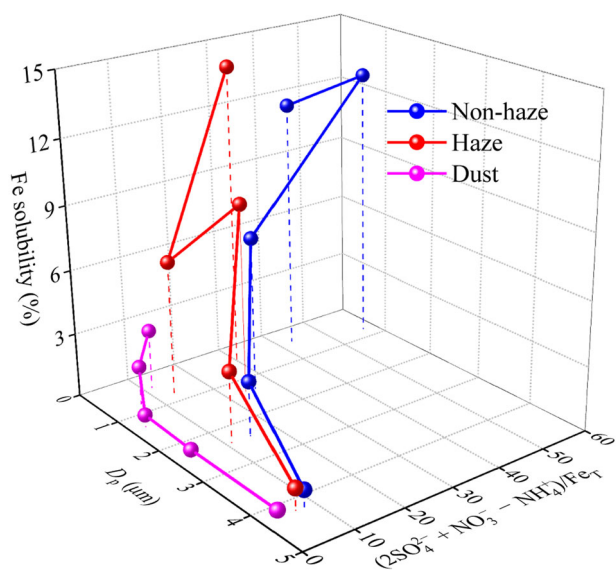


**Fig. 4 Relationships between Fe solubility and the degree of aerosol acidification, as well as particle size ( $D_p$ ) in the size range of 0.32–5.6  $\mu\text{m}$ .** The degree of aerosol acidification is indicated by the molar ratio of  $(2\text{SO}_4^{2-} + \text{NO}_3^- - \text{NH}_4^+)/\text{Fe}_T$ .

higher Fe solubility and dominated the aerosol  $\text{Fe}_D$ . The larger particles are deposited closer to the continent, whereas finer particles will be transported longer<sup>44</sup>. As a result, it is the fine-mode particles that will contribute more to ocean dissolved Fe deposition. Many recent studies (e.g., refs. <sup>19,34,45,46</sup>) considered aerosol Fe speciation from different sources in the Fe dissolution scheme and showed a higher Fe solubility in fine particles from anthropogenic aerosols than that from mineral dust. However, Ito et al.<sup>12</sup> summarized that although many atmospheric chemistry models have implemented the emissions of anthropogenic Fe sources (e.g., refs. <sup>47–52</sup>), a uniform aerosol Fe solubility is often assumed for all combustion sources and no data are available on the size distribution of Fe species in aerosol sources. Our results

suggest the need to further consider the size dependence of Fe solubility in aerosol particles derived from the aerosol acidity and aerosol Fe sources within different particle sizes, which determines how fast aerosol Fe dissolves in acidic conditions. Incorporating such new data will help models to calculate the deposition flux of dissolved Fe more accurately on the ocean surface and evaluate the impact of soluble Fe on the marine ecosystem<sup>12</sup>.

## METHODS

### Sampling site and sample collection

The field observation was conducted in the megacity Hangzhou in the Yangtze River Delta (YRD) under haze, non-haze, and dust conditions. The sampling site is located on the roof of a four-story building (30°17'N, 105°38'E, about 15 m above the ground, Supplementary Fig. 2), which well represents the mixed pollutant sources from local urban plumes and regional air masses. A 10-stage rotating micro-orifice uniform-deposit impactor (MOUDI, Model 120 R, MSP corporation, USA) was used to collect size-resolved aerosol particles at a flow rate of 30  $\text{L min}^{-1}$  with 50% cut-point aerodynamic diameters of 0.056, 0.10, 0.18, 0.32, 0.56, 1.0, 1.8, 3.2, 5.6, 10.0, and 18.0  $\mu\text{m}$ . Quartz filters (Pallflex 7204, 47-mm diameter, Pall Corporation, USA) were used as sampling substrates and thus polytetrafluoroethylene (PTFE) spacers of 0.127 cm in thickness were put in MOUDI to compensate for the jet-to-plate distance due to the use of thicker quartz substrates. Before the sample collection, all quartz filters were baked at 600  $^\circ\text{C}$  in a muffle furnace for 4 h to remove any possible contaminants. In this study, coarse- and fine-mode fractions of aerosol particles are operationally defined as larger than 1.0  $\mu\text{m}$  and between 0.056 and 1.0  $\mu\text{m}$  according to previous studies<sup>28,53</sup>.

A set of MOUDI filters were collected for 32 h during October 9–10, 2019 (haze condition with hourly  $\text{PM}_{2.5} > 35 \mu\text{g m}^{-3}$ ), for 40 h during October 12–14, 2019 (non-haze condition with hourly  $\text{PM}_{2.5} \leq 35 \mu\text{g m}^{-3}$ ), and for 46.3 h during October 29–31, 2019 (dust condition with hourly  $\text{PM}_{10} > 150 \mu\text{g m}^{-3}$  and ratio of hourly  $\text{PM}_{10}$  to  $\text{PM}_{2.5} > 3$ ). Note that the definition of haze, non-haze, and dust conditions is specific to this study. The detailed weather conditions and sampling information can be seen in Supplementary Figs. 3 and 4 and Supplementary Table 1. This dust intruded from Mongolia to the YRD on October 29, 2019 and affected Hangzhou for three consecutive days (Supplementary Fig. 5). Different stages of MOUDI filters under the dust condition are generally grayish-yellow, which is different from the gray or black filters collected under the haze condition. Furthermore, another set of field blank filters were collected following

the same procedure without running the sampler. All the quartz samples were stored at  $-20^{\circ}\text{C}$  for further analysis.

Individual particle samples were also collected on copper (Cu) transmission electron microscopy (TEM) grids coated with carbon (C) film (carbon type-B 300 mesh, Beijing XXBR Technology Co., Ltd., China) by a single-stage cascade impactor (DKL-2, Qingdao Genstar Electronic Technology Co., Ltd., China) with a 0.3 mm diameter jet nozzle and a flow of  $1.0\text{ L min}^{-1}$ . The aerodynamic diameter with 50% collection efficiency of the single-stage cascade impactor is  $0.1\ \mu\text{m}$  for the particles with a density of  $2\ \text{g cm}^{-3}$ . Individual particle samples were placed in a sealed dry plastic tube and stored at  $25^{\circ}\text{C}$  and  $20 \pm 3\%$  RH in a desiccator.

### Water-soluble inorganic ions analysis

According to the analytical procedure reported in ref. <sup>35</sup>, one-half of the MOUDI filter was cut into small pieces using ceramic scissors, put into a clean centrifuge tube with 10 ml of ultrapure water ( $18.2\ \text{M}\Omega\ \text{cm}$ ), and then ultrasonically extracted for 30 min. The extraction was filtered using a PTFE syringe filter with  $0.22\text{-}\mu\text{m}$  pores to remove insoluble aerosol components. The filtered solution was divided into two parts, one part was analyzed directly by an ion chromatography (IC) system (Dionex ICS-600, Thermo Fisher Scientific, USA) to obtain the concentrations of water-soluble ions (i.e.,  $\text{SO}_4^{2-}$ ,  $\text{NO}_3^-$ ,  $\text{Cl}^-$ ,  $\text{NH}_4^+$ ,  $\text{Ca}^{2+}$ ,  $\text{Mg}^{2+}$ ,  $\text{K}^+$ , and  $\text{Na}^+$ ) and another part was acidified immediately with ultrapure concentrated  $\text{HNO}_3$  to 0.4% (v/v)  $\text{HNO}_3$  for  $\text{Fe}_D$  analysis according to ref. <sup>15</sup>. The detection limits of  $\text{SO}_4^{2-}$ ,  $\text{NO}_3^-$ ,  $\text{Cl}^-$ ,  $\text{NH}_4^+$ ,  $\text{Ca}^{2+}$ ,  $\text{Mg}^{2+}$ ,  $\text{K}^+$ , and  $\text{Na}^+$  are 0.021, 0.008, 0.010, 0.006, 0.022, 0.009, 0.006, and  $0.018\ \mu\text{g mL}^{-1}$ , respectively. Before sample analyses, certified reference materials (Institute for Environmental Reference Materials, China) for both cations and anions were measured three consecutive times for quality control<sup>35</sup>. The detection accuracy (defined as the ratio of measured concentration divided by its certified concentration as a percentage) of  $\text{SO}_4^{2-}$ ,  $\text{NO}_3^-$ ,  $\text{Cl}^-$ ,  $\text{NH}_4^+$ ,  $\text{Ca}^{2+}$ ,  $\text{Mg}^{2+}$ ,  $\text{K}^+$ , and  $\text{Na}^+$  is  $100.6\% \pm 0.8\%$ ,  $100.1\% \pm 0.9\%$ ,  $100.5\% \pm 8.8\%$ ,  $98.5\% \pm 1.7\%$ ,  $105.4\% \pm 9.0\%$ ,  $103.4\% \pm 10.7\%$ ,  $107.8\% \pm 5.4\%$ , and  $98.5\% \pm 5.3\%$ , respectively.

### Total Fe analysis

An energy-dispersive X-ray fluorescence spectrometer (ED-XRF, Epsilon 4, PANalytical, Netherlands) was employed to determine the concentrations of total Fe and Al in each sample. Before analysis of each batch of samples, the working standard curve of ED-XRF is calibrated with the fine particulate matter standard reference material (SRM 2786, National Institute of Standards and Technology, USA). The detection accuracy of Fe and Al is  $98.9\% \pm 7.5\%$  and  $92.1\% \pm 9.8\%$ , respectively. During the ED-XRF measurement, we also analyzed three blank filters. Here, the detection limits of Fe and Al are  $0.06$  and  $0.04\ \mu\text{g cm}^{-2}$ , respectively. To guarantee that the samples do not contact any metal, a plastic tweezer was used during sample collection and analysis. The average background concentrations of Fe and Al in the blank filters are  $0.17$  and  $0.21\ \mu\text{g cm}^{-2}$ , respectively, which are much lower than those of the samples. The background values were subtracted during the data processing.

### Dissolved Fe analysis

The aforementioned acidified solutions were analyzed by inductively coupled plasma-mass spectrometry (ICP-MS, Agilent 7500ce, Agilent Technologies, USA) to determine the concentrations of  $\text{Fe}_D$  in the samples. The detailed analytical procedures can be found in ref. <sup>54</sup>. Briefly, the instrument was optimized daily by a tuning solution containing Li, Y, Tl, Ce, and Co. Calibration was conducted by external standards (Agilent Technologies, Environmental Calibration Standard). An internal standard containing  $^{45}\text{Sc}$ ,  $^{72}\text{Ge}$ ,  $^{103}\text{Rh}$ ,  $^{115}\text{In}$ ,  $^{159}\text{Tb}$ ,  $^{175}\text{Lu}$ , and  $^{209}\text{Bi}$  was added online during element analysis. The detection limit of Fe is  $2.72\ \text{ng mL}^{-1}$ .

### Individual particle analysis

Individual particle samples were analyzed using a TEM (JEM-2100, JEOL Ltd., Japan) operated at 200 kV and equipped with an energy-dispersive X-ray spectrometer (EDS, INCA X-Max<sup>N</sup> 80 T, Oxford Instruments, UK). TEM-EDS analysis can obtain physical (e.g., morphology, size, and mixing structure) and chemical (e.g., elemental composition and ratio of elements) properties of individual particles. Cu peaks in EDS spectra are excluded due to the interference from Cu substrates of TEM grids and C content may be overestimated due to the use of C film in TEM grids. TEM images were processed by the RADIUS 2.0 software (EMSI GmbH, Germany) to acquire equivalent circle diameters (ECDs) of analyzed particles.

### Calculation of enrichment factor

The enrichment factor (EF) is used to evaluate the relative contribution of natural and anthropogenic sources to elements in aerosol particles<sup>55,56</sup>. The EF method is a double normalized method by calculating the relative concentration of elements, which could eliminate the influence of variable factors, such as wind speed, wind direction, sample amount, and distance from the pollution source). The EF of element Fe ( $\text{EF}_{\text{Fe}}$ ) is calculated by choosing element Al as the reference element. The calculation formula is shown as follows:

$$\text{EF}_{\text{Fe}} = (\text{C}_{\text{Fe}}/\text{C}_{\text{Al}})_{\text{aerosol}} / (\text{C}_{\text{Fe}}/\text{C}_{\text{Al}})_{\text{crust}} \quad (1)$$

where  $(\text{C}_{\text{Fe}}/\text{C}_{\text{Al}})_{\text{aerosol}}$  represents the concentration ratio of Fe to Al in aerosols;  $(\text{C}_{\text{Fe}}/\text{C}_{\text{Al}})_{\text{crust}}$  represents the background concentration ratio of element Fe to Al in crusts. The value of  $(\text{C}_{\text{Fe}}/\text{C}_{\text{Al}})_{\text{crust}}$  used in this study is 0.44 based on the background concentrations of elements in soils of China reported in ref. <sup>57</sup>. If  $\text{EF}_{\text{Fe}}$  is close to 1, it means that the crustal source is dominant for aerosol Fe. The higher  $\text{EF}_{\text{Fe}}$  indicates the larger contribution from anthropogenic sources. If  $\text{EF}_{\text{Fe}} > 10$ , it indicates that non-crustal anthropogenic sources contribute significantly to aerosol Fe<sup>55,58,59</sup>.

### DATA AVAILABILITY

The data used in this study are available at Zenodo via <https://doi.org/10.5281/zenodo.6319476>.

Received: 15 March 2022; Accepted: 10 June 2022;

Published online: 27 June 2022

### REFERENCES

1. Tagliabue, A. et al. The integral role of iron in ocean biogeochemistry. *Nature* **543**, 51–59 (2017).
2. Ito, A. Atmospheric processing of combustion aerosols as a source of bioavailable iron. *Environ. Sci. Technol. Lett.* **2**, 70–75 (2015).
3. Shi, Z. et al. Impacts on iron solubility in the mineral dust by processes in the source region and the atmosphere: a review. *Aeolian Res.* **5**, 21–42 (2012).
4. Jickells, T. D. et al. Global iron connections between desert dust, ocean biogeochemistry, and climate. *Science* **308**, 67–71 (2005).
5. Baker, A. R. et al. Changing atmospheric acidity as a modulator of nutrient deposition and ocean biogeochemistry. *Sci. Adv.* **7**, eabd8800 (2021).
6. Mahowald, N. M. et al. Aerosol trace metal leaching and impacts on marine microorganisms. *Nat. Commun.* **9**, 15 (2018).
7. Wei, J., Yu, H., Wang, Y. & Verma, V. Complexation of iron and copper in ambient particulate matter and its effect on the oxidative potential measured in a surrogate lung fluid. *Environ. Sci. Technol.* **53**, 1661–1671 (2019).
8. Hamilton, D. S. et al. Impact of changes to the atmospheric soluble iron deposition flux on ocean biogeochemical cycles in the Anthropocene. *Glob. Biogeochem. Cycle* **34**, e2019GB006448 (2020).
9. Li, W. et al. Air pollution–aerosol interactions produce more bioavailable iron for ocean ecosystems. *Sci. Adv.* **3**, e1601749 (2017).
10. Yan, Q. et al. Emission and spatialized health risks for trace elements from domestic coal burning in China. *Environ. Int.* **158**, 107001 (2022).
11. Myriokefalitakis, S. et al. Reviews and syntheses: the GESAMP atmospheric iron deposition model intercomparison study. *Biogeosciences* **15**, 6659–6684 (2018).
12. Ito, A., Ye, Y., Baldo, C. & Shi, Z. Ocean fertilization by pyrogenic aerosol iron. *npj Clim. Atmos. Sci.* **4**, 30 (2021).
13. Ito, A. & Shi, Z. Delivery of anthropogenic bioavailable iron from mineral dust and combustion aerosols to the ocean. *Atmos. Chem. Phys.* **16**, 85–99 (2016).
14. Mahowald, N. M. et al. Atmospheric iron deposition: global distribution, variability, and human perturbations. *Annu. Rev. Mar. Sci.* **1**, 245–278 (2009).
15. Zhu, Y. et al. Iron solubility in fine particles associated with secondary acidic aerosols in east China. *Environ. Pollut.* **264**, 114769 (2020).
16. Shi, J. et al. High production of soluble iron promoted by aerosol acidification in fog. *Geophys. Res. Lett.* **47**, e2019GL086124 (2020).
17. Gao, Y. et al. Particle-size distributions and solubility of aerosol iron over the antarctic peninsula during austral summer. *J. Geophys. Res. -Atmos.* **125**, e2019JD032082 (2020).
18. Shi, Z., Krom, M. D., Bonneville, S. & Benning, L. G. Atmospheric processing outside clouds increases soluble iron in mineral dust. *Environ. Sci. Technol.* **49**, 1472–1477 (2015).
19. Fu, H. et al. Solubility of iron from combustion source particles in acidic media linked to iron speciation. *Environ. Sci. Technol.* **46**, 11119–11127 (2012).

20. Schroth, A. W., Crusius, J., Sholkovitz, E. R. & Bostick, B. C. Iron solubility driven by speciation in dust sources to the ocean. *Nat. Geosci.* **2**, 337–340 (2009).
21. Deguillaume, L. et al. Transition metals in atmospheric liquid phases: sources, reactivity, and sensitive parameters. *Chem. Rev.* **105**, 3388–3431 (2005).
22. Kuang, X. M. et al. Cloud water chemistry associated with urban aerosols: rapid hydroxyl radical formation, soluble metals, Fe(II), Fe(III), and quinones. *ACS Earth Space Chem.* **4**, 67–76 (2020).
23. Li, W. et al. Microscopic observation of metal-containing particles from Chinese continental outflow observed from a non-industrial site. *Environ. Sci. Technol.* **47**, 9124–9131 (2013).
24. Li, W. et al. Microscopic evaluation of trace metals in cloud droplets in an acid precipitation region. *Environ. Sci. Technol.* **47**, 4172–4180 (2013).
25. Oakes, M. et al. Iron solubility related to particle sulfur content in source emission and ambient fine particles. *Environ. Sci. Technol.* **46**, 6637–6644 (2012).
26. Zhang, G. et al. Source and mixing state of iron-containing particles in Shanghai by individual particle analysis. *Chemosphere* **95**, 9–16 (2014).
27. Zhou, Y. et al. Field evidence of Fe-mediated photochemical degradation of oxalate and subsequent sulfate formation observed by single particle mass spectrometry. *Environ. Sci. Technol.* **54**, 6562–6574 (2020).
28. Gao, Y. et al. Particle-size variability of aerosol iron and impact on iron solubility and dry deposition fluxes to the Arctic Ocean. *Sci. Rep.* **9**, 16653 (2019).
29. Yoshida, A. et al. Abundance and emission flux of the anthropogenic iron oxide aerosols from the East Asian continental outflow. *J. Geophys. Res. -Atmos.* **123**, 11194–11209 (2018).
30. Zhang, X. Y. et al. Atmospheric aerosol compositions in China: spatial/temporal variability, chemical signature, regional haze distribution and comparisons with global aerosols. *Atmos. Chem. Phys.* **12**, 779–799 (2012).
31. Li, W. et al. Integrated evaluation of aerosols from regional brown hazes over northern China in winter: concentrations, sources, transformation, and mixing states. *J. Geophys. Res. -Atmos.* **116**, D09301 (2011).
32. Gonet, T. & Maher, B. A. Airborne, Vehicle-derived Fe-bearing nanoparticles in the urban environment: a review. *Environ. Sci. Technol.* **53**, 9970–9991 (2019).
33. Li, S. et al. Magnetic particles unintentionally emitted from anthropogenic sources: iron and steel plants. *Environ. Sci. Technol. Lett.* **8**, 295–300 (2021).
34. Baldo, C. et al. Iron from coal combustion particles dissolves much faster than mineral dust under simulated atmospheric acidic conditions. *Atmos. Chem. Phys.* **22**, 6045–6066 (2022).
35. Xu, J. et al. An interlaboratory comparison of aerosol inorganic ion measurements by ion chromatography: implications for aerosol pH estimate. *Atmos. Meas. Tech.* **13**, 6325–6341 (2020).
36. Li, K. et al. A two-pollutant strategy for improving ozone and particulate air quality in China. *Nat. Geosci.* **12**, 906–910 (2019).
37. Liu, L. et al. Chemistry of atmospheric fine particles during the COVID-19 pandemic in a megacity of eastern China. *Geophys. Res. Lett.* **48**, e2020GL091611 (2021).
38. Sun, J. et al. Key role of nitrate in phase transitions of urban particles: implications of important reactive surfaces for secondary aerosol formation. *J. Geophys. Res. -Atmos.* **123**, 1234–1243 (2018).
39. Wang, W. et al. Sulfate formation is dominated by manganese-catalyzed oxidation of SO<sub>2</sub> on aerosol surfaces during haze events. *Nat. Commun.* **12**, 1993 (2021).
40. Zheng, G. et al. Multiphase buffer theory explains contrasts in atmospheric aerosol acidity. *Science* **369**, 1374–1377 (2020).
41. Takahama, S., Gilardoni, S. & Russell, L. M. Single-particle oxidation state and morphology of atmospheric iron aerosols. *J. Geophys. Res. -Atmos.* **113**, D22202 (2008).
42. Moffet, R. C. et al. Iron speciation and mixing in single aerosol particles from the Asian continental outflow. *J. Geophys. Res. -Atmos.* **117**, D07204 (2012).
43. Ingall, E. D. et al. Enhanced iron solubility at low pH in global aerosols. *Atmosphere* **9**, 201 (2018).
44. Seinfeld, J. H., Pandis, S. N. *Atmospheric Chemistry and Physics: From Air Pollution to Climate Change* (John Wiley & Sons, 2006).
45. Liu, M. et al. The underappreciated role of anthropogenic sources in atmospheric soluble iron flux to the Southern Ocean. *npj Clim. Atmos. Sci.* **5**, 28 (2022).
46. Zhu, Y. et al. Sources and processes of iron aerosols in a megacity in eastern China. *Atmos. Chem. Phys.* **22**, 2191–2202 (2022).
47. Ito, A. Global modeling study of potentially bioavailable iron input from ship-board aerosol sources to the ocean. *Glob. Biogeochem. Cycle* **27**, 1–10 (2013).
48. Ito, A., Lin, G. & Penner, J. E. Radiative forcing by light-absorbing aerosols of pyrogenic iron oxides. *Sci. Rep.* **8**, 7347 (2018).
49. Luo, C. et al. Combustion iron distribution and deposition. *Glob. Biogeochem. Cycle* **22**, GB1012 (2008).
50. Myriokefalitakis, S. et al. Changes in dissolved iron deposition to the oceans driven by human activity: a 3-D global modelling study. *Biogeosciences* **12**, 3973–3992 (2015).
51. Rathod, S. D. et al. A mineralogy-based anthropogenic combustion-iron emission inventory. *J. Geophys. Res. -Atmos.* **125**, e2019JD032114 (2020).
52. Wang, R. et al. Sources, transport and deposition of iron in the global atmosphere. *Atmos. Chem. Phys.* **15**, 6247–6270 (2015).
53. Zhang, H. et al. Abundance and fractional solubility of aerosol iron during winter at a coastal city in Northern China: similarities and contrasts between fine and coarse particles. *J. Geophys. Res. -Atmos.* **127**, e2021JD036070 (2021).
54. Pan, Y., Wang, Y., Sun, Y., Tian, S. & Cheng, M. Size-resolved aerosol trace elements at a rural mountainous site in Northern China: importance of regional transport. *Sci. Total Environ.* **461**, 761–771 (2013).
55. Liu, L. et al. Variations in concentration and solubility of iron in atmospheric fine particles during the COVID-19 pandemic: an example from China. *Gondwana Res.* **97**, 138–144 (2021).
56. Chester, R. et al. Factors controlling the solubilities of trace metals from non-remote aerosols deposited to the sea surface by the 'dry' deposition mode. *Mar. Chem.* **42**, 107–126 (1993).
57. Chen, J., Wei, F., Zheng, C., Wu, Y. & Adriano, D. C. Background concentrations of elements in soils of China. *Water Air Soil Poll.* **57**, 699–712 (1991).
58. Zhou, S. et al. Trace metals in atmospheric fine particles in one industrial urban city: spatial variations, sources, and health implications. *J. Environ. Sci.* **26**, 205–213 (2014).
59. Cao, J. J. et al. Size-differentiated source profiles for fugitive dust in the Chinese Loess Plateau. *Atmos. Environ.* **42**, 2261–2275 (2008).

## ACKNOWLEDGEMENTS

This work was funded by the National Natural Science Foundation of China (42075096, 42107108, and 41907186), China Postdoctoral Science Foundation (2020M681823), and Zhejiang Provincial Natural Science Foundation of China (LZ19D050001 and LY21D050002).

## AUTHOR CONTRIBUTIONS

W.L. and Z.S. conceived the study. Q.L., Y.W., and Y.Z. collected the samples. L.L., Q.L., J.Z., Q.Y., and C.B. performed the sample and data analyses. L.L. and W.L. wrote the original draft. S.Z., Z.D., W.L., and Z.S. reviewed and edited the manuscript. All the authors approved the final version of this paper.

## COMPETING INTERESTS

The authors declare no competing interests.

## ADDITIONAL INFORMATION

**Supplementary information** The online version contains supplementary material available at <https://doi.org/10.1038/s41612-022-00277-z>.

**Correspondence** and requests for materials should be addressed to Weijun Li or Zongbo Shi.

**Reprints and permission information** is available at <http://www.nature.com/reprints>

**Publisher's note** Springer Nature remains neutral with regard to jurisdictional claims in published maps and institutional affiliations.



**Open Access** This article is licensed under a Creative Commons Attribution 4.0 International License, which permits use, sharing, adaptation, distribution and reproduction in any medium or format, as long as you give appropriate credit to the original author(s) and the source, provide a link to the Creative Commons license, and indicate if changes were made. The images or other third party material in this article are included in the article's Creative Commons license, unless indicated otherwise in a credit line to the material. If material is not included in the article's Creative Commons license and your intended use is not permitted by statutory regulation or exceeds the permitted use, you will need to obtain permission directly from the copyright holder. To view a copy of this license, visit <http://creativecommons.org/licenses/by/4.0/>.

© The Author(s) 2022